ORIGINAL ARTICLE

Exploration on reduced graphene oxide/strontium pyro niobate electrode material for electrochemical energy storage applications

M. Infant Shyam Kumar[1,2] · **S. Shahil Kirupavathy**[3] ⬤ · **S. Shalini**[4]

Abstract

Most recently, graphene-related composite-modified electrode surfaces are been widely employed to improve surface interactions and electron transfer kinetics. Hydrothermally prepared strontium pyro niobate (SPN) and reduced graphene oxide/ strontium pyro niobate (RGOSPN) nanostructures reveal excellent morphology. X-ray diffraction analysis of SPN and RGOSPN agree with standard data. Thermogravimetry–differential scanning calorimetry analyses show that RGOSPN has higher thermal stability than SPN. In addition, from the polarization–electric field (P–E) loop measurements, the estimated value of remnant polarization (P_r) and coercive electric field (E_c) of SPN are 0.039 µC cm^{-2} and -2.90 kV cm^{-1} and that of RGOSPN nanocomposite are 0.0139 µC cm^{-2} and -2.04 kV cm^{-1}. Cyclic voltammetry measurements show that RGOSPN nanocomposite manifests the possibility of electrochemical reversibility beyond long cycles without change in performance. The redox cycle reveal that RGOSPN can be used as part of a composite electrode for hybrid capacitors dynamic conditions. Moreover, the specific capacitance of SPN and RGOSPN was calculated using galvanostatic charge–discharge (GCD) technique. The observed energy density of 9.1 W h kg^{-1} in RGOSPN is higher when compared with previous reported values.

Keywords Hummer's method · Hydrothermal method · Nanocomposites · Columbite · Electrochemical studies · Impedance spectroscopy

1 Introduction

Development of novel technology for sustainable energy production and affordable health care system are the significant challenges among researchers in the recent days. Electrochemistry plays a substantial role in several chemical and biological sensors as well as energy storage devices. This utilizes energy as electricity to gather or inoculate electrons through electrodes in clean form. Recently, graphene-supported metal, metal oxides and polymer has gathered much interest in developing bifunctional catalyst for energy conversion system [1].

Columbite compounds are found with a combination of fascinating physical properties such as piezoelectric, magnetic, catalytic, photovoltaic, ferroelectric and dielectric [2, 3]. These properties make them suitable for a wide range of applications. Columbites have also put into the energy conversion process as active electrode materials to enhance the composite behavior, owing to its high electronic and ionic conductivity [4–7]. Columbite ferroelectric materials are significant materials identified by the presence of a change in spontaneous polarisation in accordance with applied external electric field. Ferroelectrics usually include titanates, zirconates and niobates which are structure-dependent type [8].

Graphene, an allotrope of carbon plays a significant role in all aspects such as energy storage devices, energy generation devices, catalysts, sensor fabrication, and cost-effective water purification. Advanced graphene-based materials always bring new perspectives and prospects to the electrochemical systems. Graphene has been incorporated along with columbite to improve electrochemical performance of the composites. Strontium pyro niobate with

✉ S. Shahil Kirupavathy
   shahilkirupavathy@yahoo.co.in

1. Department of Physics, Rajalakshmi Engineering College, Chennai 602105, India

2. Faculty of Technology, Anna University, Chennai 600025, India

3. Department of Physics, Velammal Engineering College, Chennai 600066, India

4. Department of Physics, R.M.D. Engineering College, Kavaraipettai 601206, India

chemical formula $Sr_2Nb_2O_7$ exhibit orthorhombic crystal structure with space group Cmc21 and belong to the ferroelectric material and possess high Curie temperature, with very high thermal and chemical stability. This material also exhibits appreciable piezoelectric and electro-optic properties [9–14].

Recently graphene-based heterostructures offers new opportunities for the development of energy storage devices and for the stabilization of conceptually new two-dimensional materials. To bridge better understanding between experimental approach and theoretical approach about the graphene composite structure formation, computational methods can also be adopted for the characterization of graphene-based composite derivatives. Interplay of gas phase, atomistic, electronic processes and surface reactions about graphene-based composite structure can be regulated by density-functional ab initio molecular dynamics with van der Waals corrections beyond the resolution of experimental techniques [15]. Theoretical calculations can also be used to investigate mechanism from the electronic level, which could provide an explanation for some experimental phenomenon [16, 17].

Herein, we describe a hydrothermal route for the synthesis of strontium pyro niobate (SPN) rhombic nanosheets. Morphological evolution of nanostructures was obtained by maintaining reaction at low temperature in alkaline (sodium hydroxide) medium. We also established a unique structured composite material consisting of SPN sheets and reduced graphene oxide (RGO) by hydrothermal method. Distinctly, the facile hydrothermal method produces homogeneous nanostructured columbite materials with sheet-like morphology. This nanostructured-reduced graphene oxide strontium pyro niobate (RGOSPN) composite material was characterized physicochemically and electrochemically as a new kind of bifunctional catalyst for energy storage devices. Crystallite size of SPN and RGOSPN materials were studied with the help of X-ray diffraction (XRD) and high-resolution scanning electron microscopy (HRSEM). In addition, ferroelectric properties of the composite prepared were investigated at ambient condition. Electrochemical analysis both by cyclic voltammetry and galvanostatic charging and discharging methods were carried out to analyze the suitability of the composite for energy storage applications.

2 Experimental

2.1 Materials

Graphite powder, $KMnO_4$ (99%), H_2SO_4 (98%), $SrCl_2 \cdot 6H_2O$ (99%), Nb_2O_5 (99.95%), NaOH (97%) H_2O_2 (30% concentration) and HCl (35% concentration) were purchased from Sisco research laboratory. Milli-Q (Millipore, Milford, MA)

water was used throughout the experiment. All other chemicals, reagents and solvents utilized in this experiment were of analytical grade.

2.2 Synthesis of graphene oxide and strontium pyro niobate

Modified Hummer's method was adopted to derive graphene oxide (GO) [18]. High vapor pressure condition obtaining hydrothermal method was appropriated to synthesize SPN. Optimized synthesis was promoted by mixing 0.266 g of $SrCl_2 \cdot 6H_2O$ and 0.266 g of Nb_2O_5 (1:1), in 9 g of NaOH (2 M) alkaline solution with constant stirring for 30 min. The solution mixture was then transferred into a 150-ml Teflon-lined stainless steel autoclave and the temperature was allowed to maintain at 200 °C for 24 h. The reaction mixture obtained under hydrothermal condition was then taken out and rinsed several times using de-ionized (DI) water and centrifuged several times in well-dispersed 10% diluted HCl at 6000 rpm to remove impurities present in the obtained reaction mixture. Finally, dried compound was sintered using a silica crucible at 700 °C for 20 h using a high-temperature furnace.

2.3 Preparation of reduced graphene oxide/ strontium pyro niobate nanocomposite

GO and SPN powder in 1:1 weight ratio was dispersed well in 25 ml ethanol and 15 ml DI water. The pH of the mixture was estimated as 12. The obtained mixture was stirred for 30 min and ultrasonicated for 30 min to obtain uniform dispersant. The stirred solution was then taken into a 150-ml stainless steel autoclave lined with Teflon and heated at 180 °C for 2 h and subsequently cooled to room temperature. The obtained materials were then rinsed thoroughly with DI water followed by 10% diluted HCl and centrifuged many times at 6000 rpm to remove the impurities present in the prepared nanocomposite. The resulting material was further dried at 80 °C for 2 h.

2.4 Characterization tools

XRD studies of SPN and RGOSPN samples were performed on a Rigaku smart lab X-ray diffractometer, coupled with 3 kW X-ray generator Cu tube, using radiation ($\lambda = 1.5406$ Å) with 2θ ranging from 5° to 90° at a step scanning of 0.02°. Morphologies of the prepared samples were analyzed using high-resolution scanning electron microscopy (HRSEM)-(FEI Quanta FEG 200 equipped with energy-dispersive analysis of X-rays). Spectral analysis was carried out using Perkin Elmer FTIR instrument (scan range 4000–450 cm^{-1}) adopting globar and mercury as source and BRUKER RFS 27: stand-alone FT–Raman

Spectrometer (scan range 4000–50 cm^{-1}) with 1064 nm Nd–YAG laser source. Thermal stability of the synthesized materials were measured by thermogravimetric (TG) and differential scanning calorimetry (DSC) using NETZSCH5 simultaneous TG analyzer, by heating the specimens from 35 to 1400 °C in nitrogen at 10 °C min^{-1}. Ferroelectric hysteresis data (P–E loop) were collected using 609E−6 high-voltage amplifier interfaced with 4 kV radiant technologies at room temperature.

The electrochemical properties of graphite rod, SPN and RGOSPN samples were evaluated using the three-electrode system in 0.1 M H_2SO_4 medium using the electrochemical workstation (Biological-SP240). Platinum and calomel electrodes were used as the counter and reference electrode, respectively. SPN/RGOSPN, carbon black and polyvinylpyrrolidone (PVP) were taken in the weight ratio of 70:20:10 for the preparation of slurry. The solvent used for the preparation of slurry was N-methyl-2-pyrrolidone (NMP). Slurry of SPN/RGOSPN was coated on the surface of the carbon paper separately as a thin layer by slurry casting method [19]. The net mass of active coating material was 0.5 mg cm^{-2}. The net mass of active coating material was about 0.5 mg cm^{-2}. This prepared working electrode of SPN and RGOSPN were kept in a hot air oven maintained at 80 °C for 12 h for drying and desiccated overnight. Cyclic voltammetry (CV) data were obtained with electrochemical workstation (Biologic-SP240) for various scan rates (10, 20, 30, 40, 50, 60, 80, and 100 mV s^{-1}) between −0.2 and 1.0 V in acidic medium. The carbon paper-modified SPN and RGOSPN working electrodes were used for impedance measurement using Biologic-SP 240 apparatus.

3 Results and discussion

3.1 X-ray diffraction analysis

The XRD pattern of GO, SPN and RGOSPN are shown in Fig. 1a–c. The prominent diffraction peak spotted at $2\theta = 11.58°$ having an interlayer distance of 0.76 nm along the (001) orientation in Fig. 1a suggests the oxidation of graphite which is the formation of GO [20]. The peak also confirms the exfoliation of GO sheets from graphite flakes.

Figure 1b shows the XRD pattern of as-synthesized SPN nanopowder. The obtained planes were indexed for orthorhombic structure with lattice constant $a = 3.933$ Å, $b = 26.572$ Å and $c = 5.679$ Å [21]. The obtained pattern is in agreement with the standard JCPDS data card (file no. 70-0114). Intense peaks of SPN are observed at $2\theta = 29.35°$ and 32.32° and are related to (131) and (151) planes, respectively. The crystallite size of SPN nanopowders was evaluated as an average of 90 nm, by adopting Scherrer's equation and the prominent peaks [22].
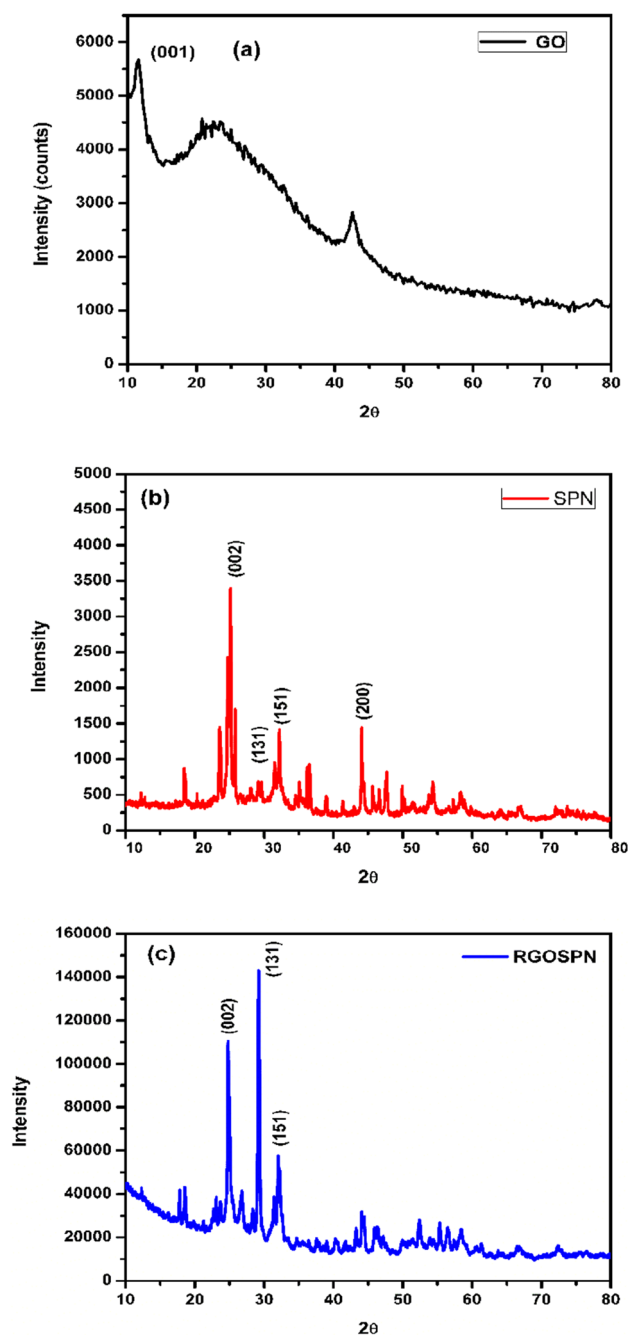

Fig. 1 Diffraction pattern of **a** GO, **b** SPN, and **c** RGOSPN

XRD pattern of RGOSPN nanocomposite is shown in Fig. 1c. The major peak at 24.80° confirmed the presence of RGO and is indexed as (002). The existence of SPN is revealed by the increased intense peak at $2\theta = 29.35$ and 32.32 corresponding to (131) and (151) planes, respectively [23]. The average crystallite size of RGOSPN was estimated as 61 nm using the Scherrer's equation and the prominent peak values.
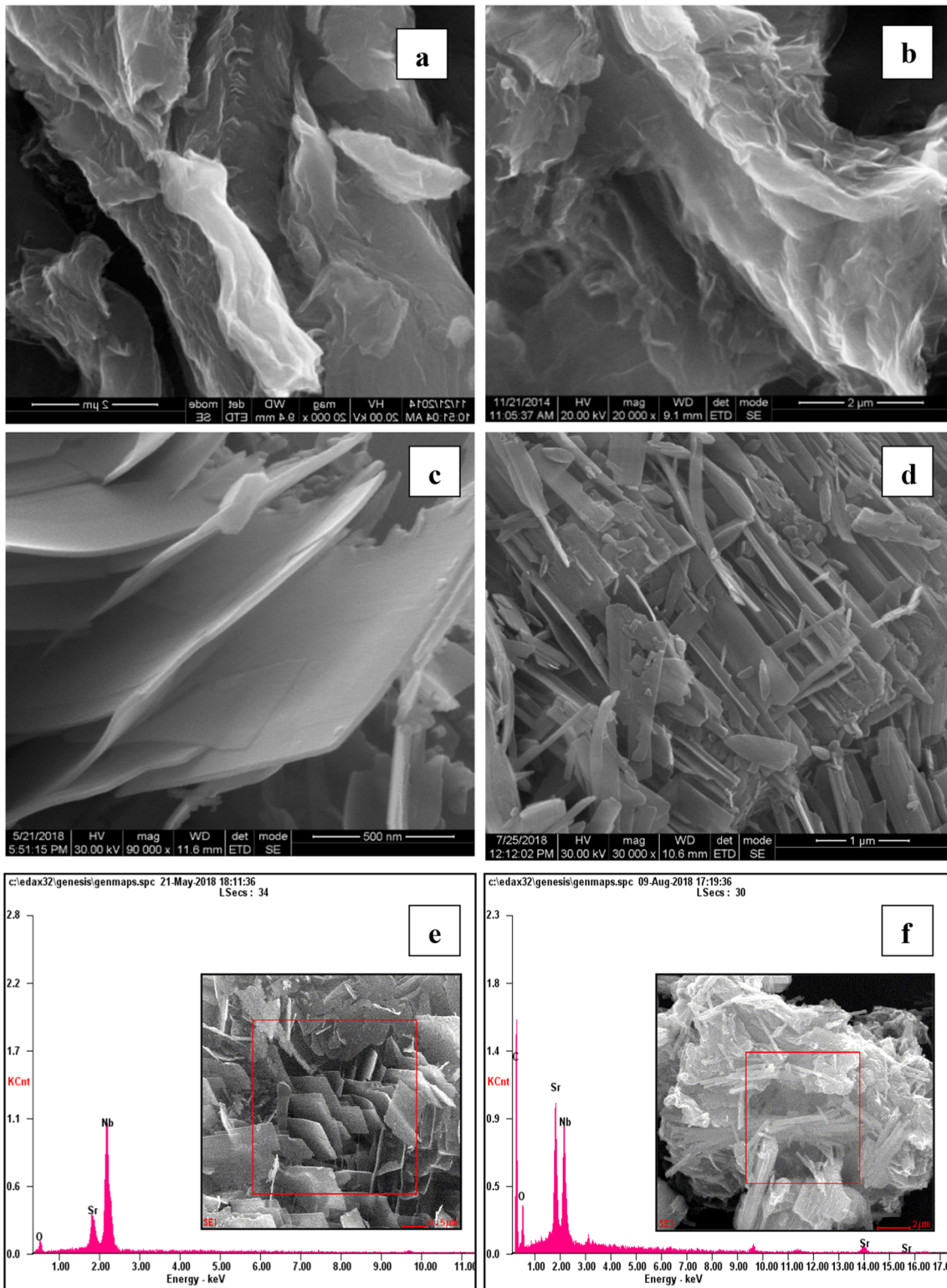
Fig. 2 Morphology of **a**, **b** GO, **c** SPN, and **d** RGOSPN and compositional analysis of **e** SPN and **f** RGOSPN composite

Table 1 Elemental composition of SPN

Element	Wt%	At%
OK	20.22	59.28
NbL	64.91	32.77
SrL	14.86	7.96
Matrix	Correction	ZAF

Table 2 Elemental composition of RGOSPN

Element	Wt%	At%
CK	74.86	87.09
OK	12.56	10.97
NbL	07.46	01.12
SrL	05.12	00.82
Matrix	Correction	ZAF

3.2 Morphological and composition studies

HRSEM analyses were carried out for GO, SPN and RGOSPN samples to determine the surface morphology. Morphology of GO images showed in Fig. 2a, b unveiled that the exfoliated GO material comprised of crumpled sheets, aggregated randomly and closely associated with each other. In addition, thin sheets are formed from the graphite solid. The crinkled and folded regions of the exfoliated sheets of 2-nm average widths were identified by HRSEM [24].

Figure 2c presents the morphology of the SPN nanopowder obtained from hydrothermal method at 200 °C for 24 h. Shapeless structure was obtained under hydrothermal condition at 200 °C for 2 h. Upon increasing the reaction time to 24 h and at higher pH 12 condition, nanosized sheet-like morphology with an amorphous phase appeared [25]. The observed crystallite size ranged from 90 to 500 nm and matched well with XRD results.

In Fig. 2d, we see image of nanocomposite RGOSPN. This figure very clearly reveals that SPN nanosheets are linked with functionalized graphene. Moreover, grain size of the composite is modified with nanostructured SPN sheets and compared with XRD results. Thus, compound novelty is been established from the morphological analysis.

The EDAX characterization of SPN and RGOSPN are shown in Fig. 2e, f. Figure 2e and inset picture confesses that the sheet-like particles are most probably comprised of three elements such as strontium, niobium and oxygen, with the exclusion of carbon. After the reduction of graphene oxide with nanostructured SPN through hydrothermal condition, EDAX analysis in Fig. 2f and inset figure shows the inclusion of carbon with strontium niobium oxide. Elemental compositional analysis of SPN and RGOSPN are compiled in Tables 1 and 2.

3.3 Spectral analysis

3.3.1 FTIR spectral analysis

The presence of different functional groups in GO such as O–H, C–OH, C–O and COOH is observed in Fig. 3a, the FTIR spectra of GO [26]. The FTIR spectra of SPN and RGOSPN are presented in Fig. 4a, b. In the FTIR spectra of SPN shown in Fig. 4a, the intensities of the FTIR bands in the region between 1000 and 400 cm^{-1} clearly establish bending and stretching modes of NbO_6 octahedron [27]. The peaks at 856, 704, 508 cm^{-1} explicit v_1 (B_{2u}) mode, v_2 (B_{2u}) mode and v_3 (B_{2u}) mode of vibration, respectively, and is observed due to stretching and bending modes of NbO_6 octahedra [28].

In the spectra corresponding to RGOSPN shown in Fig. 3a, the overlapping of B_{1u}, B_{2u}, and B_{3u} symmetries are identified. The broad prominent peak at 664 cm^{-1}
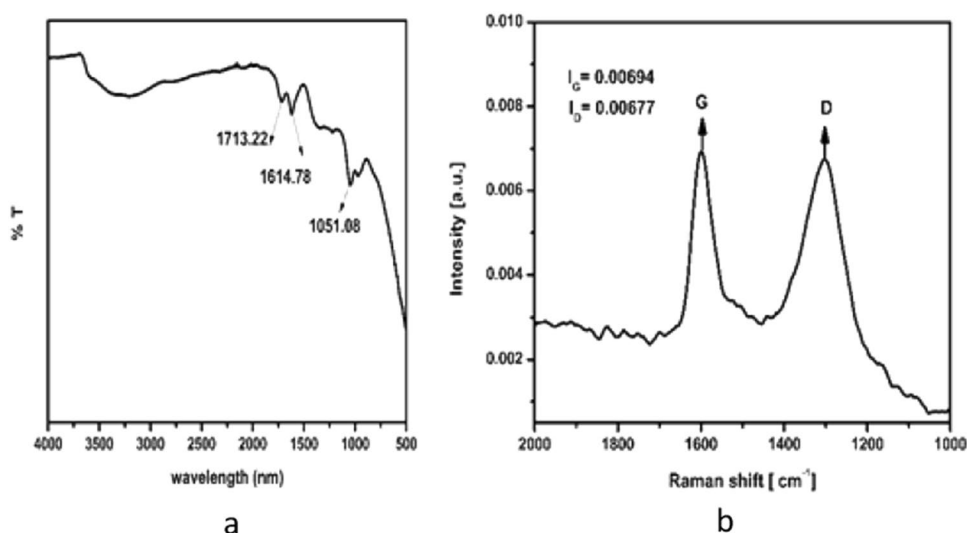
Fig. 3 **a** FTIR spectra of GO and **b** Raman spectra of GO

a

b

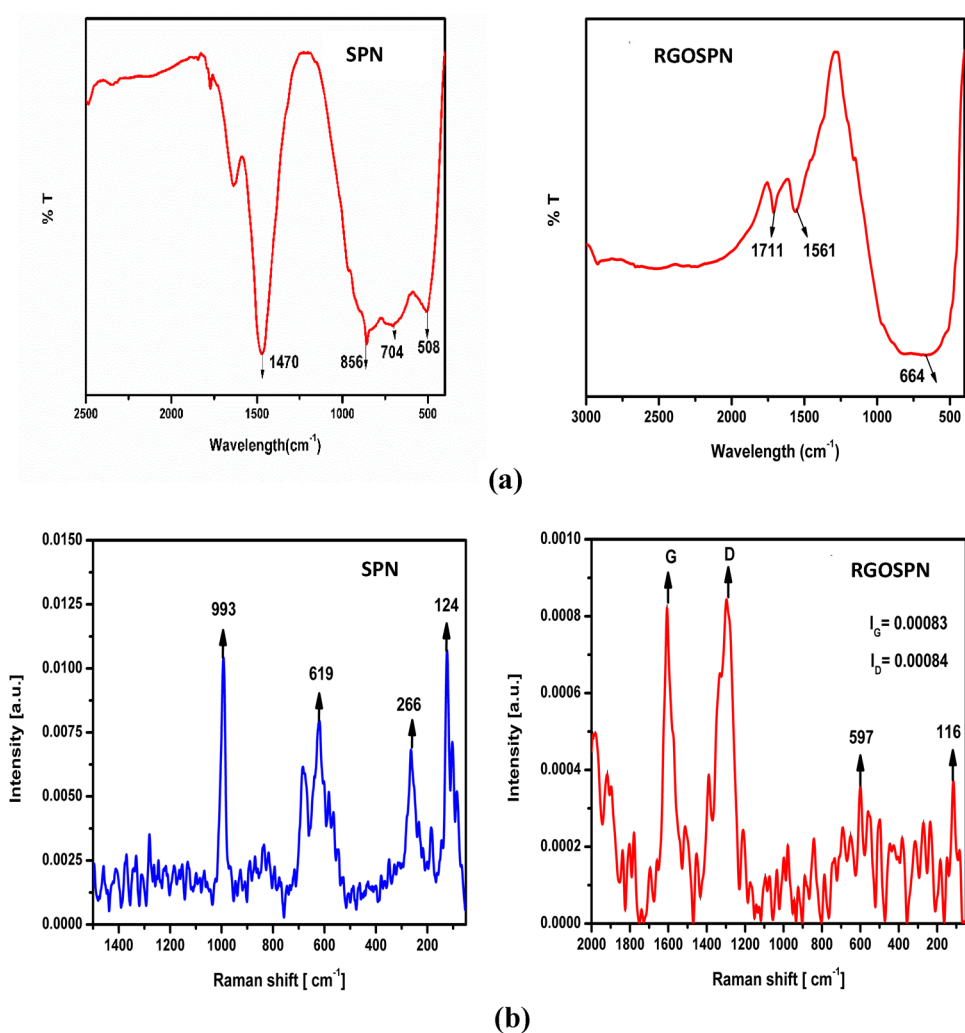**Fig. 4** **a** FTIR spectra of SPN and RGOSPN and **b** Raman spectra of SPN and RGOSPN

(a)

(b)

Table 3 FTIR spectral assignments of GO, SPN and RGOSPN

GO (cm^{-1})	SPN (cm^{-1})	RGOSPN (cm^{-1})	Assignment
3000–3500			~OH
1713		1711, 1561	~C=O
1614			~C=C
1051			~C–O–C
	856, 704, 508	664	~Nb–O

indicate the vibrations of Nb–O (stretching). Furthermore, shift in wavelength at 1711 and 1561 cm^{-1} due to stretch of carbonyl, carboxyl groups and the broadening of the vibrational peaks designating a slightly distorted (NbO$_6$ octahedra) crystal structure confirms the reduction of GO and also the attachment of RGO with polycrystalline SPN. The observed IR bands and the band assignments are compiled in Table 3.

3.3.2 FT–RAMAN spectral analysis

Raman spectroscopy stays as an effective tool to identify structural changes and analyze the characteristic modes associated with nanocomposites due to its sensitivity to local symmetry. The Raman spectra show both *D* and *G* ply as prominent peaks for all composite material based on carbon. The *G* bands are harmonized to the first-order scattering of the E_{2g} mode in the Brillouin zone of sp^2 carbon bonding and the *D* bands corresponds to structural defects. Raman spectra of GO presents in the previous reported article describes the C–C bond stretching in sp^2 carbon system seen at 1599 cm^{-1} corresponds to the *G* band and the availability of sp^2 carbon system disorder visible at 1303 cm^{-1} confirms the *D* band [26, 29]. Estimated intensity ratio of the *D* band to the *G* band ($I_D/I_G = 0.8781$) provides information of the defects and validates the shift of carbon atoms from sp^2 to sp^3 hybridized carbon after oxidation.

Raman spectra of SPN and RGOSPN are plotted in Fig. 3b. In Raman spectra of SPN shown in Fig. 4b,

phonons of strong intensity active modes at 993, 619, 266 and 124 cm^{-1} are consigned to the fundamental vibrations of the NbO_6 octahedron. The sharp intense band at 993 cm^{-1} [v_1 (A_1g) mode] is attributed to the terminal Nb–O stretching vibration. The prominent peak at 619 cm^{-1} corresponds to F_{2g} mode and bridge Nb–O stretching vibration and the peak at 121 cm^{-1} exhibits the chain Nb–O stretching vibration. The bending vibration of O–Nb–O occur in the range of 450–100 cm^{-1} [30].

According to Monisha et al. [31], defective *D* band occurs due to the disordered arrangement of carbon atoms and that of *G* band arises due to the tangential stretching vibrations of carbon atoms in GO. Thermal reduction of GO to rGO, reduced the number of carboxylic acid, ether and hydroxyl groups and caused a decrease in intensity of *D* band in RGOSPN when compared to that of GO. In addition, a shift in both *D* and *G* bands in RGOSPN is noticed. Further, the Raman spectra of RGOSPN shown in Fig. 3b give the intensity ratio of *D* and *G* bands as 1.01. The increase in *D/G* intensity ratio from 0.8781 to 1.01 interprets that single layer of graphene has interlinked (as described in HRSEM analysis) with the nanostructured SPN and exhibits bridge and chain Nb–O stretching vibration mode (F_{2g}) consigned at 597 and 116 cm^{-1}, respectively. This shift in *D* and *G* band shift in peak of Nb–O_6 vibrations when composite is formed is well witnessed in the Raman spectra of previously reported composite materials such as $NiNb_2O_6$-rGO, $CuNb_2O_6$-rGO and $ZnNb_2O_6$-rGO [32, 33]. Moreover, in the current study after the decoration of SPN with RGO, shift in peak of Sr–O_6 and Nb–O_6 vibrations is noticed. In addition, the presence of rGO was further confirmed in RGOSPN composites with a small rise of peak around ~ 1400 to ~ 1500 cm^{-1}.

Further, the Raman spectra of RGOSPN shown in Fig. 4b, gives the intensity ratio of *D* and *G* bands as 1.01. The increase in *D/G* intensity ratio from 0.8781 to 1.01 interprets that single layer of graphene has interlinked (as described in HRSEM analysis) with the nanostructured SPN and exhibits bridge and chain Nb–O stretching vibration mode (F_{2g}) consigned at 597 and 116 cm^{-1} respectively.

3.4 Thermal analysis of GO, SPN and RGOSPN

The thermal graph shown in Fig. 5a shows a gradual weight loss (6.43%) due to decomposition of functional groups having oxygen in GO (–C=O, –COOH, and OH) with a strong exothermic peak at 218.4 °C. The thermal stability of SPN and RGOSPN composite is analyzed from Fig. 5b, c. In the TG–DSC curve of SPN, we see a gradual weight loss from 100 to 700 °C and this can be attributed to the separation of the labile oxygen-containing functional groups and H_2O vapor from the material due to annihilation of oxygenated functional groups. In addition, the DSC curve in Fig. 5b communicates a

strong endothermic peak at 863 °C revealing the decomposition of SPN. When graphene is incorporated into SPN, the prominent endothermic peak is shifted to 1348.7° exhibiting very high thermal stability and is seen in Fig. 5c.

3.5 Ferroelectric studies

The *P–E* loop of SPN and RGOSPN samples were obtained at room temperature for an applied electric field of 1 kV cm^{-1} and is shown in Fig. 6a, b. The *P–E* loop is partially saturated due to the applied low electric field. The curve also intimates the excellent ferroelectric behavior of the SPN and RGOSPN nanostructure. The spontaneous polarization (P_s) for SPN nanosheets is 0.1041 μC cm^{-2}, while the corresponding remanent polarization (P_r) and coercive electric field (E_c) are 0.039 μC cm^{-2} and − 2.90 kV cm^{-1}, respectively. The coercive electric field (E_c) at room temperature for RGOSPN is − 2.04 kV cm^{-1}. This observed reduction in coercive electric field of RGOSPN when compared with SPN is due to the addition of graphene. The spontaneous polarization (P_s) and remanent polarization (P_r) for RGOSPN nanocomposite observed at the measuring electric field of 1 kV are ~ 0.0622 and 0.0139 μC cm^{-2}, respectively. Further, the area of the RGOSPN loop is observed to be less when compared with SPN. This reveals that the remanent polarization of RGOSPN nanomaterial has been enhanced with better consistency and also confirms the ferroelectric nature of the composite. The squareness of polarization calculated using the following relation gives a value of 0.3230 and 0.4719 for SPN and RGOSPN, respectively:

$$R_{sq} = \frac{P_r}{P_s} + \frac{P_{1.1E_c}}{P_r}. \tag{1}$$

3.6 Electrochemical measurement of SPN and RGOSPN

Cyclic voltammogram provides a time-dependent current (*I*) which is plotted against the scanned potential (*E*) and yields a cyclic voltammogram (CV) curve for capacitive diagnosis [34]. The CV analysis was carried out in acidic medium to reveal the reversible system. The net mass of active material on carbon paper was 0.5 mg cm^{-2}. To explore electrochemical surface reaction of SPN and RGOSPN working electrode, cyclic voltammetry was carried out at different scan rates.

3.6.1 Cyclic voltammetry

Cyclic voltammetry (CV) measurements were carried out in 0.1 M H_2SO_4 medium to analyze the electrochemical performances of the two samples namely SPN and RGOSPN.

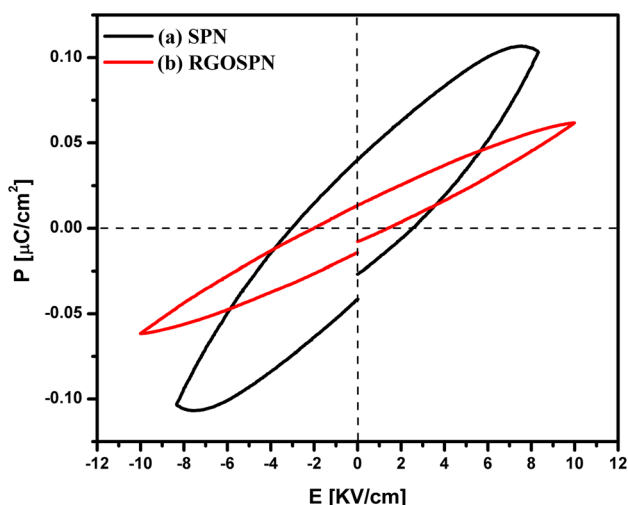**Fig. 5** TG and DSC curve of **a** GO, **b** SPN, and **c** RGOSPN
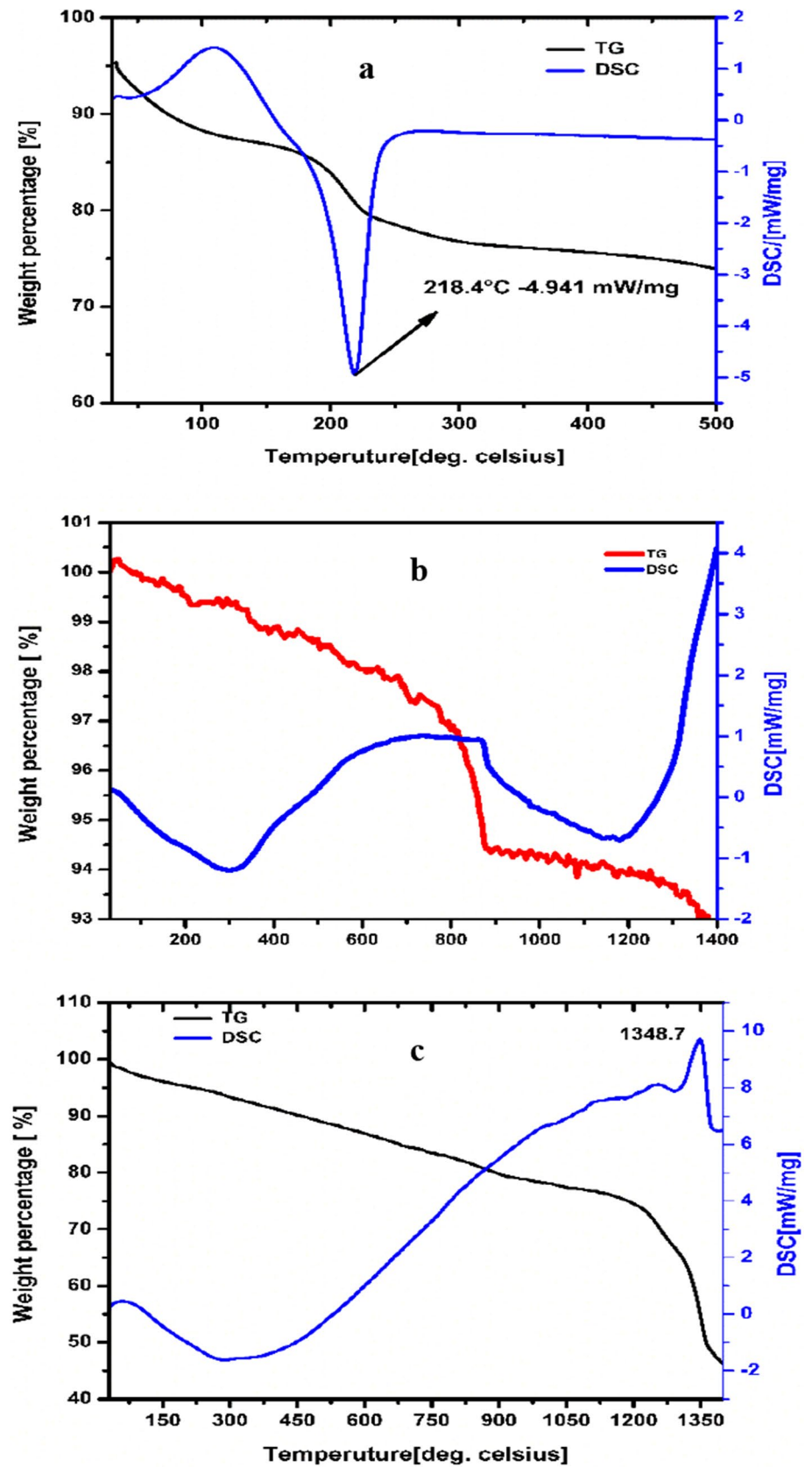
Fig. 6 *P–E* loops of **a** SPN and **b** RGOSPN

Both the samples were analyzed within the potential range of −0.2 to +1 V for a scan rate of 10, 20, 30, 40, 50, 60, 80 and 100 m V s^{-1}. The potential window for the columbite SPN and RGOSPN electrode is thus 1.2 V.

Figure 7a, b shows the CV curves for SPN and RGOSPN samples, respectively. The CV curves for SPN and RGOSPN shows that the overall area under the curve increases with increase in scan rate owing to increase in the value of current. At higher scan rate, the redox peaks get shifted. The reduction peak approaches the lower potential whereas the oxidation peak approaches the higher potential value. The rate of migration of ions and electrons at the electrode–electrolyte interface will be fast at higher scan rate for which the current value is high [35]. The shift which is noticed at higher scan rate reflects that electronic neutralization could not get satisfied. The redox reaction of SPN is represented by the following equation:
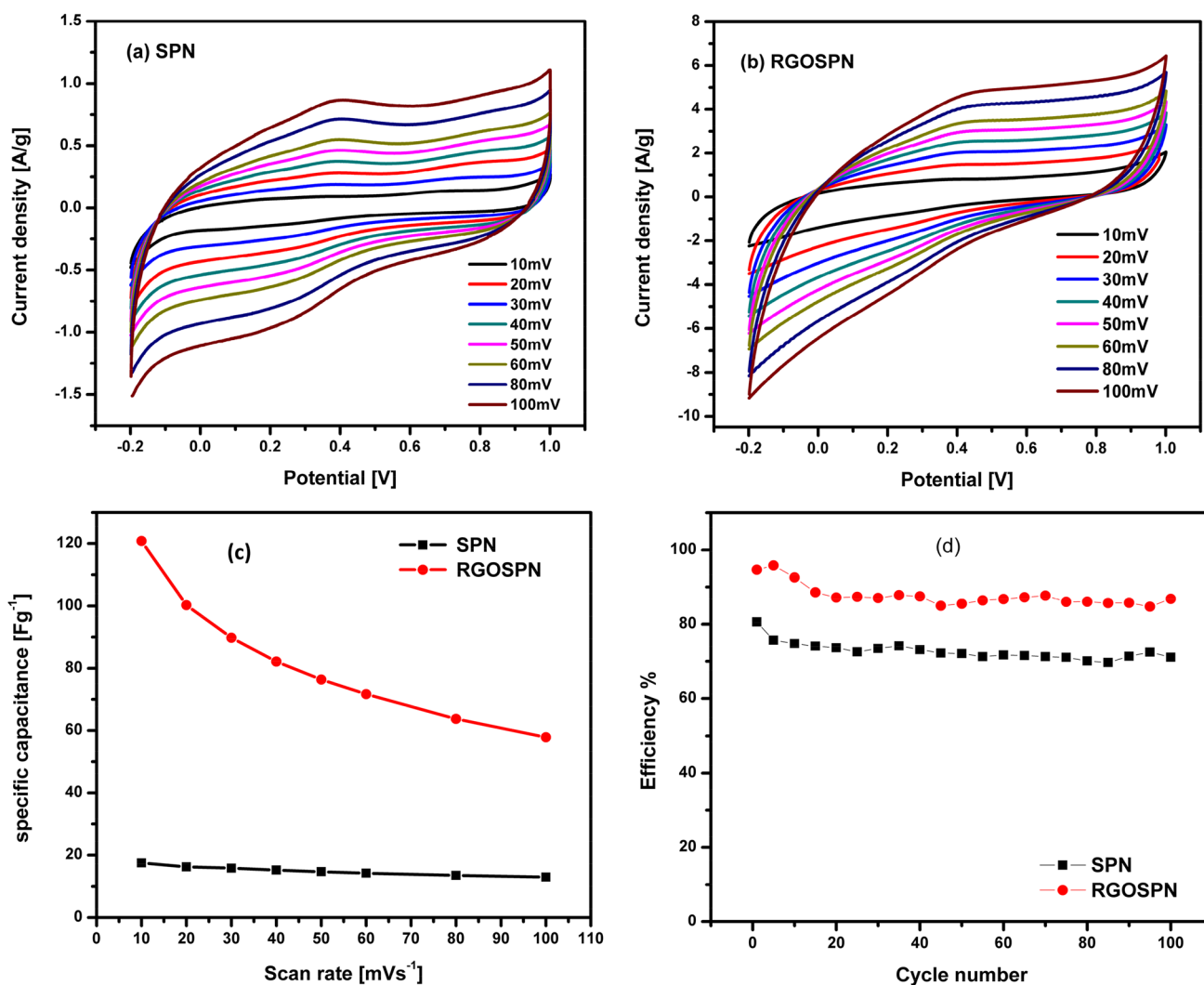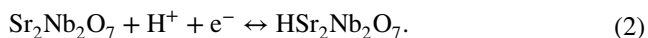

Fig. 7 Cyclic voltammetry in 0.1 M H$_2$SO$_4$ of **a** SPN and **b** RGOSPN. **c** Variation of specific capacitance as a function of scan rate for SPN and RGOSPN and **d** performance comparison of SPN and RGOSPN-modified electrode

$$\mathrm{Sr_2Nb_2O_7 + H^+ + e^- \leftrightarrow HSr_2Nb_2O_7.} \qquad (2)$$

The specific capacitance of SPN and RGOSPN samples were estimated using the relation:

$$C_{sp} = \frac{\int I\, dV}{vmV}, \qquad (3)$$

where I denotes the response current, V refers to potential window, v is the recorded scan rate in millivolts per second and m refers to mass of active material on electrode [36].

The calculated specific capacitance for different scan rate presented in Table 3 clearly indicates that the value of specific capacitance decreases with increase in scan rate. At lower scan rate, the electrolyte ions have sufficient time to diffuse and reach the pores within the material and this in turn enable to expose the active material. However, at high scan rates, the material at the electrode surface is not able to contribute to the process because of the insufficient time for the electrolyte ions to penetrate into the pores. A decrease in capacitance is clearly demonstrated with increase in scan rate. The electrochemical performance of RGOSPN sample under the mentioned conditions is presented in Fig. 7b. The incorporation of RGO into SPN has shown an increase in the redox peak. The increase in current is attributed to the increased electrical conductivity due to the reduction of graphene oxide with SPN [37].

RGO sheets usually suffer from agglomeration, porous and restacking due to the van der Waals interactions, which leads to a loss of effective ion-accessible surface area and consequently a lower capacitance than as expected. This behavior and the existence of abnormal redox peaks rather than rectangular shape can be attributed to the redox reaction of OH– with the residual functional groups such as epoxy, hydroxyl, and carboxyl function groups in the RGO [38]. In addition, this behavior relatively displays the partial reduction of graphene oxide. Some of the oxygen functional groups in RGOSPN are essentially electrochemical active and thereby oxidization or reduction may be abnormal even at mild electrochemical potentials.

Volumetric capacitances for graphene-based composite electrode materials are usually less than 200 F cm^{-3}, due to their low packing density. Instability of ion-accessible surface area arises due to contents of oxygenated groups in RGO, including C–OH, C=O, and –COOH not easily controlled by most common reduction methods. Surface functionalization is an effective tool to solve the above-mentioned challenges. Surface functional groups containing oxygen, fluorine, nitrogen, sulfur boron, or phosphorus could not only enhance the pseudocapacitance, but also increase the wettability of the electrode material and further increase the ion-accessible surface area [39].

Figure 7c shows the variation of specific capacitance (C_s) with scan rate for SPN and RGOSPN. It is noted that in the case of both SPN and RGOSPN, the specific capacitance decreases with increase in scan rate owing to the transfer rate of electrolytes. This further leads to either depletion or saturation of ions in the electrolytes inside the electrode during the redox process. When the transfer of electrolyte ions become faster, it makes hydrogen ions insertion into the nanocomposites easier [40].

However, while comparing the specific capacitance of SPN with RGOSPN we see an increase in the specific capacitance when RGO was incorporated into SPN. The addition of reduced graphene oxide into SPN has increased the value of specific capacitance of RGOSPN which is well evidenced from Table 4.

To determine the cyclic stability, the potential window was maintained at a range of -0.2 to 1.0 V. For 100 cycles, the scan rate was set at a rate of 10 m V s^{-1}. The observed output is shown in Fig. 7d. From Fig. 7c, we understand that at the end of 100 cycles, the RGOSPN binary nanocomposites retain 85% of its initial capacitance value which is higher than SPN. The excellent cyclic stability of RGOSPN with superior reversibility is thus established.

3.6.2 Galvanostatic charge–discharge (GCD) analysis

Galvanostatic charge–discharge analysis was carried out to study the GCD performance for various current densities. Figure 8a, b displays the charge–discharge behavior exhibited by SPN and RGOSPN composite electrodes between 0 and 1 V for current density value of 1, 2, and 3 Ag^{-1} in 0.1 M H$_2$SO$_4$ aqueous solution.

The charge–discharge curves of SPN and RGOSPN very clearly show that the voltage decreases along with the discharge time and this describes pseudocapacitance and hybrid capacitance. The discharge curve of SPN composite measured at low current density shown in Fig. 8a consists

Table 4 Specific capacitance of SPN and RGOSPN nanostructures measured at different scan rates

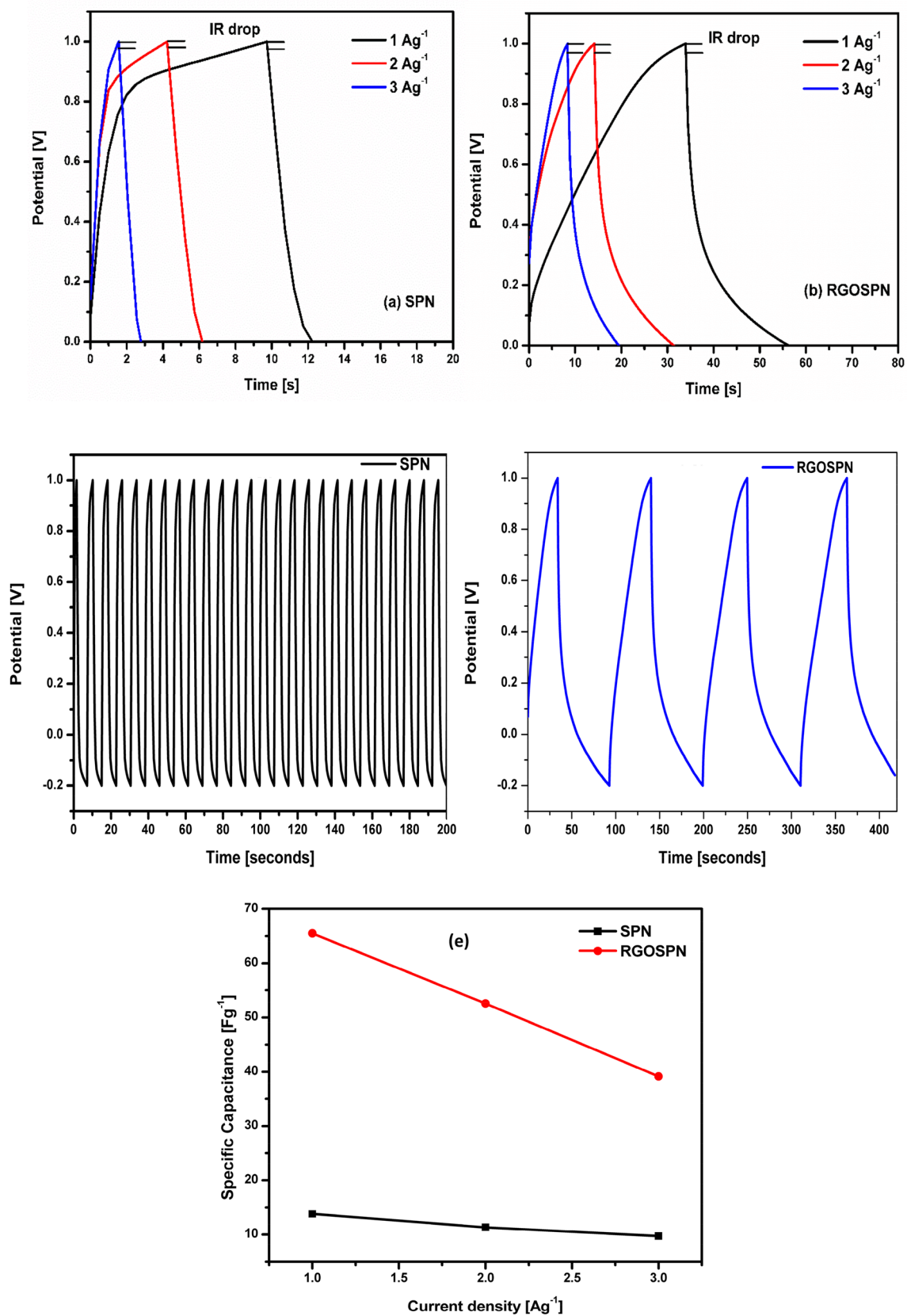| Scan rate (mV s^{-1})	Specific capacitance (Fg^{-1}) SPN	Specific capacitance (Fg^{-1}) RGOSPN
10	17.50	120.83
20	16.25	100.25
30	15.83	89.78
40	15.20	82.12
50	14.67	76.36
60	14.22	71.69
80	13.50	63.75
100	12.95	57.83

Fig. 8 GCD charging/discharging profile of **a** SPN and **b** RGOSPN electrode, cyclic stability using GCD of **c** SPN and **d** RGOSPN. **e** Variation of specific capacitance with current density SPN and RGOSPN

of a sudden potential drop from 1.0 V. This potential drop represents a typical pseudocapacitance nature, caused by electrochemical adsorption/desorption or a redox reaction at the electrode/electrolyte interface [41]. However, a slight curvature from 0.3 to 0 V indicates slow charge/discharge duration, which is a typical pseudocapacitance behavior due to double-layer distribution. Usually, Faradaic redox reaction is accompanied by the double-layer charge discharge process, and thus the combination of electric double-layer capacitance and Faradaic pseudocapacitance is responsible for hybrid capacitance [42].

The larger specific capacitance value of the RGOSPN composite than the pure SPN further proves that the combination of graphene anchored with sheet-like SPN is very beneficial for improving the storage performance. Subsequently, the GCD properties of the composite were obtained with different current density of H_2SO_4 electrolytes.

The drop in voltage in GCD curve is due to internal resistance, and due to capacitance. To observe effective capacitance from GCD curve, constant current interval is noticed at the moment the discharge process initiated [43]. Further, the IR drop is calculated from the difference between the second discharge point to the beginning of discharge for various current density such as 1 Ag^{-1}, 2 Ag^{-1} and 3 Ag^{-1}. Specific capacitance was also evaluated by subtracting the IR drop for the similar current density mentioned above using the following equation and values are listed in Table 5:

$$C_{sp} = \frac{I \, dt}{m \, dV},\tag{4}$$

where C_{sp} refers to specific capacitance possessed by the active material; I, dt, dV, and m are constant discharge current (A), discharge time (s), the voltage changes after a full discharge (V), and the mass of active material (g), respectively [44]. It is found that the specific capacitance of SPN and RGOSPN electrode based on the as-prepared composite reached a maximum value of 13.80 Fg^{-1} and 65.50 Fg^{-1}, respectively, in 0.1 M H_2SO_4 electrolyte for a current density of 1 Ag^{-1}. The enhancement in specific capacitance of RGOSPN was observed when GO was reduced with SPN owing to the higher discharge time and is identified from Fig. 8b. The results are in good agreement with the results obtained from the cyclic voltammetry.

The stability of SPN and RGOSPN nanomaterials were determined by GCD technique for 100 cycles and is presented in Fig. 8c, d. RGOSPN binary nanocomposite retains higher discharge time than SPN. This demonstrates the acceptable cyclic stability and specific capacitance of the material with superior reversibility.

Figure 8e displays the variation in specific capacitance of the SPN and hybrid RGOSPN for different current densities of 1, 2 and 3 Ag^{-1}. The work carried out by Zhao et al. reveal that RGO material when made as a supercapacitor electrode, the film exhibits a gravimetric specific capacitance of 42.5 Fg^{-1} at 1 Ag^{-1} in 0.1 M H_2SO_4 aqueous electrolyte when integrated into a symmetric cell [45]. In the present study, SPN exhibit 23.62 Fg^{-1} at 1 Ag^{-1} and RGOSPN exhibit 73.27 Fg^{-1} at 1 Ag^{-1} thus revealing that the electrochemical performance of hybrid RGOSPN electrode is superior to SPN electrode.

The energy density (E_s) and power density (P_s) of SPN and RGOSPN were estimated from the following relation:

$$E_s = \frac{1}{2}\left(\frac{C_s \times dV^2}{3.6}\right),\tag{5}$$

$$P = \left(\frac{3600 \times E_s}{dt}\right),\tag{6}$$

where E_s refers to energy density (W h kg^{-1}), dV refers to potential window (V), C_s refers to specific capacitance (F g^{-1}), P is power density (W kg^{-1}) and dt refers to discharge time (s). The maximum energy density and power density of about 1.91 W h kg^{-1} and 665.6 W kg^{-1} were computed for SPN at 1 Ag^{-1} current density. Moreover, the maximum energy density and power density of about 9.1 W h kg^{-1} and 463.9 W kg^{-1} were calculated for RGOSPN composite for the same current density. Table 6 shows the relative comparison of energy density value of RGOSPN with other supercapacitor materials. From table, it is well evident that this composite electrode RGOSPN demonstrates relatively good energy density than conventional capacitors, delivering power density significantly higher than the common fuel cell and battery.

Table 5 Specific capacitance of SPN and RGOSPN by GCD mode

Current density (Ag^{-1})	Specific capacitance (Fg^{-1})	
	SPN	RGOSPN
1	23.62	73.27
2	21.53	60.67
3	13.30	59.68

Table 6 Comparison of energy density and power density of RGOSPN with other supercapacitor materials

Material	Reference	Energy density (W h kg^{-1})	Power density (kW kg^{-1})
$NiCO_2O_4$/AC	Ding et al. [42]	6.8	2.8
Co_3O_4@MnO_2/Activated Graphene	Lei et al. [46]	17.7	0.6
$NiCO_2O_4$–MnO_2/AC	Kuang et al. [47]	5.8	2.5
RGOSPN	Present work	9.1	0.464

3.6.3 Impedance spectroscopy

Electrochemical impedance spectroscopy (EIS) test for SPN and RGOSPN were performed at room temperature in the frequency range of 100 Hz to 7 MHz with 10 mV AC sine amplitude to evaluate the electrochemical behavior.

The obtained typical Nyquist plot for the samples is presented in Fig. 9a, b. The impedance spectra were analyzed by the Z fit analysis using the EC-lab software available in the instrument. The resulting parameters are presented in Table 7 and the obtained equivalent circuit is shown as inset in Fig. 8a, b. It is observed from the plot that the data resemble the shape of a capacitive straight line nearer to $-\mathrm{Im}$ (Z). Further, the Nyquist plots of bare SPN and RGOSPN nanocomposite show a semi-circle with greater diameter and semi-circle with shorter diameter, respectively. Here, Z'' denotes the imaginary component of the impedance and Z' denotes the real component of impedance. The diameter of semi-circle indicates the interfacial charge transfer resistance. The significant decrease in diameter of semi-circle demonstrates promising electrochemical properties in RGOSPN nanocomposite when compared to SPN nanostructure. The vertical line observed at the low-frequency region in RGOSPN reveals the process of diffusion of ions in the electrolytes and adsorption on the graphite sheet-modified electrodes [48].

The SPN system shows the data modeled with one simple series R_2W_2 circuit connected parallel with a capacitor (C_2) and R_1 connected in series as seen in Fig. 9a. C_2 element of SPN system was computed as 14.53 Fg^{-1}. The resistances R_1 and R_2 in SPN equivalent circuit represent the contact resistance and the material layer resistance. These resistances are in general present in all practical devices.

The RGOSPN system reflects an enhancement in C_2 element value as 72.4 Fg^{-1} which is much greater than the observed in SPN. In addition, the RGOSPN system possess one simple series R_2W_2 circuit connected parallel with a capacitor (C_2) and connected in series with resistance R_1 as shown in Fig. 8b. RGO when composited with SPN enables to improve the dielectric property and electrical conductivity. The obtained capacitive straight line for SPN at high-frequency illustrates pseudo capacitance. However, the addition of RGO on SPN shows enhanced hybrid capacitance at high frequency [49].

The EIS data were further used to analyze the electrochemical properties of SPN and RGOSPN nanocomposite in the frequency range from 0.1 kHz to 100 kHz under open circuit potential. The EIS data were modified into specific capacitance using the relation:
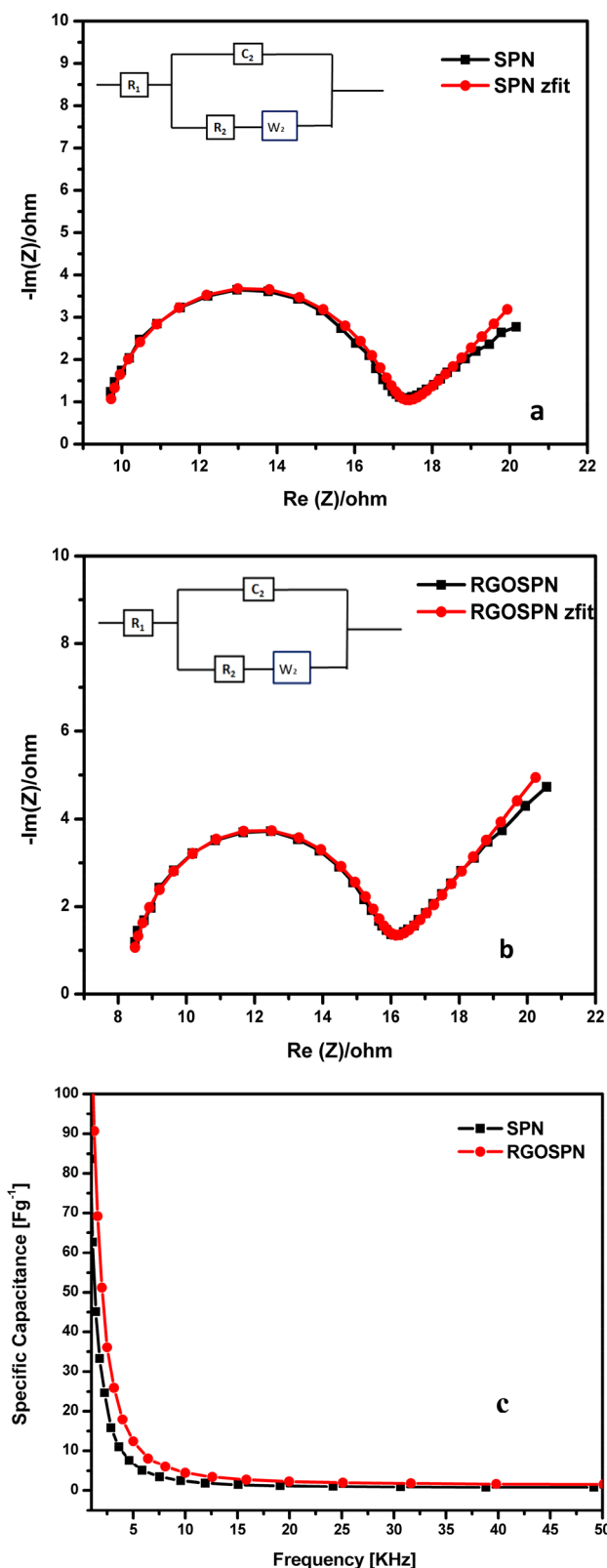
$$C_s = -(2\pi f Z'')^{-1} \tag{7}$$

Fig. 9 Nyquist plots and normalized Z fit of **a** SPN and **b** RGOSPN and **c** Bode impedance plot from EIS data exhibiting variation of specific capacitance with frequency

Table 7 Circuit parameters of SPN and RGOSPN

Circuit parameters	Observed values	
	SPN	RGOSPN
R1	$9.56\ \Omega$	$8.266\ \Omega$
R2	$7.235\ \Omega$	$7.045\ \Omega$
C2	$14.53\ \mathrm{Fg^{-1}}$	$72.4\ \mathrm{Fg^{-1}}$
W2	$43.36\ \Omega\ \mathrm{s^{-1/2}}$	$67.66\ \Omega\ \mathrm{s^{-1/2}}$

Z'' indicates imaginary part of impedance and f indicates the measurement frequency [48]. The modifying impedance data into capacitance and its outcomes are displayed in Fig. 9c. It is well illustrated in the figure that specific capacitance (C_s) decreases with increasing frequency and this behavior is well agreed with the decrease in capacitance with increase in scan rate during the cyclic voltammetry analysis (Fig. 7c).

4 Conclusion

In this work, SPN was prepared through hydrothermal approach. The morphological analysis reveals that sheet-like SPN structure is well dispersed and anchored on flexible graphene sheets. The synthesized RGOSPN unique nanostructure is thermally stable up to 1348.7 °C as observed from TG–DSC analysis. Polarization of RGOSPN was also analyzed using P–E loop. The remarkable electrochemical performance of RGOSPN revealed in CV analysis is owing to the unique nanostructure of RGOSPN. The specific capacitance of SPN and RGOSPN were estimated using the CV technique and GCD technique. The estimated specific capacitance value of RGOSPN reveals that addition of graphene on stable SPN, has greatly improved its specific capacitance to 120.83 $\mathrm{Fg^{-1}}$ at 10 mV $\mathrm{s^{-1}}$ in 0.1 M H_2SO_4. The estimated energy density and power density of 1.91 W h $\mathrm{kg^{-1}}$ and 665.6 W $\mathrm{kg^{-1}}$ at 1 $\mathrm{Ag^{-1}}$ current density in SPN was enhanced greatly to a value of 9.1 W h $\mathrm{kg^{-1}}$ and 463.9 W $\mathrm{kg^{-1}}$ for RGOSPN composite at 1 $\mathrm{Ag^{-1}}$ current density. Energy density and power density of RGOSPN were also compared with reported materials. Analysis on suitability of RGOSPN as an active material revealed that it exhibits promising hybrid capacitance, reversibility and good redox behavior in acidic medium. Thus, the RGOSPN binary component will play a vital role for making it a promising electrode material for the hybrid capacitance nature.

References

1. Li R, Wei Z, Gou XL (2015) Nitrogen, phosphorus dual-doped graphene/carbon nanosheets as bifunctional electrocatalysts for oxygen reduction and evolution. ACS Catal 5:4133–4142
2. Prokhorov AM, Kuzminov YS (1990) Ferroelectric crystals for laser radiation control, vol 81. Adam Hilger, Bristol
3. Deshpande SB, Potdar HS, Godbole PD, Date SK (1992) Preparation and ferroelectric properties of SBN:50 ceramics. J Am Soc Ceram 75:2581–2585
4. Yang W, Salim J, Li SH, Sun C, Chen L, Goodenough JB, Kim Y (2012) Perovskite $Sr_{0.95}Ce_{0.05}CoO_{3−\delta}$ loaded with copper nanoparticles as a bifunctional catalyst for lithium-air batteries. J Mater Chem 22:18902–18907
5. Garcia EM, Tarôco HA, Matencio HT, Domingues RZ, Dos Santos JAF (2012) Electrochemical study of $La_{0.6}Sr_{0.4}Co_{0.8}Fe_{0.2}O_3$ during oxygen evolution reaction. Int J Hydrog Energy 37:6400–6406
6. Jin C, Cao XC, Lu F, Yang Z, Yang R (2013) Electrochemical study of $Ba_{0.5}Sr_{0.5}Co_{0.8}Fe_{0.2}O_3$ perovskite as bifunctional catalyst in alkaline media. J Hydrog Energy 38:10389–10393
7. Sunarso J, Torriero AAJ, Zhou W, Howlett PC, Forsyth M (2012) Oxygen reduction reaction activity of La-based perovskite oxides in alkaline medium: a thin-film rotating ring-disk electrode study. J Phys Chem C 116:5827–5834
8. Mendesa RG, Araújob EB, Eirasc JA (2001) Structural characterization and ferroelectric properties of strontium barium niobate ($Sr_xBa_{1−x}Nb_2O_6$) thin films. Mater Res 4:113–116
9. Nanamatsu S, Kimura M, Doi K, Takahashi M (1971) Ferroelectric properties of $Sr_2Nb_2O_7$ single crystal. J Phys Soc Jpn 30:300–301
10. Takahashi M, Nanamatsu S, Kimura M (1972) The growth of ferroelectric single crystal $Sr_2Nb_2O_7$ by means of the floating zone technique. J Cryst Growth 13–14:681–685
11. Nanamatsu S, Kimura M, Kawamura T (1975) Crystallographic and dielectric properties of ferroelectric $A_2B_2O_7$ (A = Sr, B = Ta, Nb) crystals and their solid solutions. J Phys Soc Jpn 38:817–824
12. Shabbir G, Kojima S (2003) Acoustic and thermal properties of strontium pyroniobate single crystals. J Phys D Appl Phys 36:1036–1039
13. Ishizawa N, Marumo F, Kawamura T, Kimura M (1975) The crystal structure of $Sr_2Nb_2O_7$, a compound with perovskite-type slabs. Acta Crystallogr B31:1912–1915
14. Daniels P, Tamazyan R, Kuntscher CA, Dressel AM, Lichtenberg F, Van Smaalen S (2002) The incommensurate modulation of the structure of $Sr_2Nb_2O_7$. Acta Crystallogr B 58:970–976
15. Sangiovanni DG, Gueorguiev GK, Kakanakova-Georgieva A (2018) Ab initio molecular dynamics of atomic-scale surface reactions: insights into metal organic chemical vapor deposition of AlN on graphene. Phys Chem Chem Phys 20:17751–17761
16. Goyenola C, Stafström S, Schmidt S, Hultman L, Gueorguiev GK (2014) Carbon fluoride, CFx: structural diversity as predicted by first principles. J Phys Chem C 118(12):6514–6521
17. Zhang H, Du X, Ding S, Wang Q, Chang L, Ma X, Hao X, Pen C (2019) DFT calculations of the synergistic effect of λ-MnO_2/Graphene composites for electrochemical adsorption of lithium ions. Phys Chem Chem Phys 21:8133–8140
18. Zaaba NI, Foo KL, Hashim U, Tan SJ, Liu WW, Voon CH (2017) Synthesis of graphene oxide using modified hummers method: solvent influence. Procedia Eng 184:469–477
19. Kandalkar S, Dhawale D, Kim C, Lokhande C (2010) Chemical synthesis of cobalt oxide thin film electrode for supercapacitor application. Synth Met 160:1299–1302
20. Jabbar A, Yasin G, Khan WQ, Anwar MY, Korai RM, Nizam MN, Muhyodin G (2017) Electrochemical deposition of nickel graphene composite coatings: effect of deposition temperature

on its surface morphology and corrosion resistance. RSC Adv 7:31100–31109

21. Atuchin VV, Grivel JC, Korotkov AS, Zhang Z (2008) Electronic parameters of $Sr_2Nb_2O_7$ and chemical bonding. J Solid State Chem 181:1285–1291

22. Patterson AL (1939) The Scherrer formula for X-ray particle size determination. Phys Rev J 56:978–982

23. Veerappan G, Yoo SY, Zhang K, Ma M, Kang B (2016) High-reversible capacity of perovskite $BaSnO_3$/rGO composite for lithium-ion battery anodes. Electrochem Acta 214:31–37

24. Gurunathan SJ, Han JW, Park JH, Kim E, Choi YJ, Kwon DN (2015) Reduced graphene oxide–silver nanoparticle nano-composite: a potential anticancer nanotherapy. Int J Nanomed 10:6257–6276

25. Cho I-S, Lee S, Noh JH, Kim DW, Jung HS, Kim DW, Hong KS (2010) Facile hydrothermal synthesis of $SrNb_2O_6$ nanotubes with rhombic cross sections. Cryst Growth Des 10:2447–2450

26. Kumar MIS, Kirupavathy SS, Jerusha E, Sureshkumar S, Vinolia M (2018) Synthesis and characterization of novel reduced graphene oxide supported barium niobate (RGOBN) nanocomposite with enhanced ferroelectric properties and thermal stability. J Mater Sci Mater Electron 29:19228–19237

27. Ke QQ, Wang J (2016) Graphene-based materials for supercapacitor electrodes—a review. J Materiomics 2:37–54

28. Mathai KC, Vidya S, John A, Solomon S, Thomas JK (2014) Structural, optical, and compactness characteristics of nanocrystalline $CaNb_2O_6$ synthesized through an auto igniting combustion method. Adv Condens Matter Phys. https://doi.org/10.1155/2014/735878

29. Song Z, Liu W, Wei W, Quan C, Sun N, Zhou Q, Liu G, Wen X (2016) Preparation and electrochemical properties of Fe_2O_3/reduced graphene oxide aerogel (Fe_2O_3/rGOA) composites for supercapacitors. J Alloy Compd 685:355–363

30. Alanis J, Rodríguez-Aranda MC, Rodríguez ÁG, Ojeda-Galván HJ, Mendoza ME, Navarro-Contreras HR (2019) Temperature dependence of the Raman dispersion of $Sr_2Nb_2O_7$: influence of an electric field during the synthesis. J Raman Spectrosc 50:102–114

31. Monisha M, Priyadarshani N, Durairaj M, Sabari Girisun TC (2020) 2PA induced optical limiting behaviour of metal (Ni, Cu, Zn) niobate decorated reduced graphene oxide. Opt Mater 101:109775

32. Arunkumar P, Ashish AG, Babu B, Sarang S, Suresh A, Sharma CH, Shaijumon MM (2015) Nb_2O_5/graphene nanocomposites for electrochemical energy storage. RSC Adv 5(74):59997–60004

33. Li X, Zhang T, Gu S, Kang SZ, Li G, Mu J (2013) Reduced graphene oxide/potassium niobate composite nanoscrolls with enhanced photocatalytic activity for dye degradation. Sep Purif Technol 108:139–142

34. Elgrishi N, Rountree KJ, McCarthy BD, Rountree ES, Eisenhart TT, Dempsey JL (2018) A practical beginner's guide to cyclic voltammetry. J Chem Educ 95:197–206

35. Kim BK, Sy S, Yu A, Zhang J (2015) Electrochemical supercapacitors for energy storage and conversion. Handbook of clean energy systems. Wiley, New York. ISBN:978-1-118-38858-7

36. Ghosh D, Giri S, Moniruzzaman M, Basu T, Mandala M, Das CK (2014) αMnMoO₄/graphene hybrid composite: high energy density supercapacitor electrode material. Dalton Trans 43(28):11067–11076

37. Yuan L, Lu XH, Zhai T, Dai J, Zhang F, Hu B, Wang X, Gong L, Chen J, Hu C, Tong Y, Zhou J, Wang ZL (2012) Flexible solid-state supercapacitors based on carbon, nanoparticles/MnO_2 nanorods hybrid structure. ACS Nano 6:656–661

38. Wang HW, Hu ZA, Chang YQ, Chen YL, Zhang ZY, Yang YY, Wu HY (2011) Preparation of reduced graphene oxide/cobalt oxide composites and their enhanced capacitive behaviors by homogeneous incorporation of reduced graphene oxide sheets in cobalt oxide matrix. Mater Chem Phys 130:672–679

39. Liu Z, Wang LD, Ma G, Yuan Y, Jia HN, Fei W (2020) Supercapacitor with ultrahigh volumetric capacitance produced by self-assembly of reduced graphene oxide through phosphoric acid treatment. J Mater Chem A 8:18933–18944

40. Liu J, Shakir I, Kang DJ (2014) Lithium niobate nanoflakes as electrodes for highly stable electrochemical supercapacitor devices. Mater Lett 119:84–87

41. Kim CH, Kim B-H, Yang KS (2012) TiO_2 nanoparticles loaded on graphene/carbon composite nanofibers by electrospinning for increased photocatalysis. Carbon 50:2472–2481

42. Ding R, Qia L, Jiac MJ, Wang H (2013) Facile and large-scale chemical synthesis of highly porous secondary submicron/micron-sized $NiCo_2O_4$ materials for high-performance aqueous hybrid AC-$NiCo_2O_4$ electrochemical capacitors. Electrochim Acta 107:494–502

43. Azhagan MVK, Vaishampayan MV, Shelke MV (2014) Synthesis and electrochemistry of pseudocapacitive multilayer fullerenes and MnO_2 nanocomposites. J Mater Chem A 2:2152

44. Chen T, Dai L (2014) Flexible supercapacitors based on carbon nanomaterials. J Mater Chem A 2(28):10756

45. Zhao Y, Liu J, Wang B, Sha J, Li Y, Zheng D, Amjadipour M, MacLeod J, Motta N (2017) Supercapacitor electrodes with remarkable specific capacitance converted from hybrid graphene oxide/NaCl/urea films. ACS Appl Mater Interfaces 9(27):22588–22596

46. Lei Z, Zhang J, Zhao XS (2012) Ultrathin MnO_2 nano fibers grown on graphitic carbon spheres as high-performance asymmetric supercapacitor electrodes. J Mater Chem 22:153–160

47. Kuang M, Wen ZQ, Guo XL, Zhang SM, Zhang YX (2014) Engineering firecracker-like beta-manganese dioxides@spinel nickel cobaltates nanostructures for high-performance supercapacitors. J Power Sources 270:426–433

48. Aadil M, Shaheen W, Warsi MF, Shahid M, Khan MA, Ali Z, Haider S, Shakir I (2016) Superior electrochemical activity of α-Fe_2O_3/rGO nanocomposite for advance energy storage devices. J Alloy Compd 689:648–654

49. Sumboja A, Foo CY, Wang X, Lee PS (2013) Large areal mass, flexible and free-standing reduced graphene oxide/manganese dioxide paper for asymmetric supercapacitor device. Adv Mater 25:2809–2815